RAPID COMMUNICATIONS

PHYSICAL REVIEW E VOLUME 51, NUMBER 6 JUNE 1995

Heat front propagation in femtosecond-laser-heated solids

A. Ng and A. Forsman
Physics Department, University of British Columbia, Vancouver, British Columbia, Canada V6T 1Z1

P. Celliers
Lawrence Livermore National Laboratory, Livermore, California 94550

(Received 18 January 1995)

The formation and propagation of heat fronts produced by an intense femtosecond-laser pulse are examined in numerical simulations which treat self-consistently laser absorption, thermal conduction, and hydrodynamics. The results revealed that the initial heat front is dictated by laser absorption as an evanescent wave. The effect of thermal conduction becomes important as the temperature of the solid increases. The results also suggest that such heat fronts may be used to probe the electrical and thermal conductivities of hot, dense plasmas.

PACS number(s): 52.25.Fi, 52.25.Rv, 52.40.Nk, 52.50.Jm

Heating of a solid by intense femtosecond lasers offers new possibilities for investigating hot, dense plasmas. Earlier work on self-reflectivities has focused on the study of plasma electrical conductivity [1–3]. Recently, reflectivity and Doppler shift measurements have been made on heat fronts produced in a transparent solid [4]. A glass slab with a top layer of 300 Å of carbon is irradiated with a 100-fs, 616-nm pulse at 5×10^{14} W/cm^2. The heat front observed in the transparent material is interpreted as the result of thermal conduction from the carbon layer, which drives a supersonic ionization wave into the glass slab. The process is analyzed using a simple nonlinear heat wave model with Spitzer thermal conductivity [5].

In this paper, we will examine the formation and propagation of heat fronts produced by intense femtosecond-laser pulses in solids using a one-dimensional numerical calculation which treats self-consistently the processes of laser absorption, electron thermal conduction, and hydrodynamics. It is found that the initial propagation of the heat front is dominated by the laser deposition as an evanescent wave. This is governed by the plasma electrical conductivity. As the temperature of the solid increases, electron thermal conduction becomes important. The nonlinear heat flow leads to steepening of the heat front. At later times, hydrodynamics begins to take effect, driving a compressional wave which coalesces with the thermal wave and propagates as a decaying shock. These suggest that measurements of the heat front may be used to probe both the thermal and electrical conductivities of hot dense plasmas.

In the numerical model, we consider a laser pulse incident from vacuum onto aluminum at normal incidence. Aluminum is chosen because of the widest range of available data and models on its physical properties. Since the primary interest is on dense plasmas, normal incidence is used to minimize the gradient scale length of the plasma on the target surface and to avoid laser-plasma coupling at the critical density layer by resonance absorption for P-polarized radiation.

The deposition of laser radiation and the dynamics of the resulting plasma are calculated self-consistently by solving the Helmholtz equations for electromagnetic waves [6] and the fluid equations for conservation of mass, momentum, and energy in a one-dimensional hydrodynamic code [7]. The cold solid and the subsequent hot plasma are described by a complex dielectric function $\varepsilon(z,t)=1+i4\pi\sigma(\omega)/\omega$, where $\sigma(\omega)$ is the electrical conductivity. At each time step, the Helmholtz equations are solved to satisfy boundary conditions corresponding to an incident and a reflected wave in the vacuum, and an evanescent wave in the target.

The frequency-dependent electrical conductivity is obtained from the Drude approximation of $\sigma(\omega)=\omega_p^2/4\pi(\nu_{ei}-i\omega)$, where $\omega_p^2=4\pi Z^* n_i e^2/m_e$ is the plasma frequency, Z^* the average ionization state, n_i the ion density, m_e the electron mass, and e the electron charge. The electron-ion collision rate ν_{ei} is given by $Z^* n_i e^2/m_e\sigma_0$ and the dc electrical conductivity σ_0 is obtained from the models of Lee and More [8], Rinker [9], or Perrot and Dharma-wardana [10]. Z^* is calculated using a screened hydrogenic model [11] in the work of Lee and More and using an atom-in-jellium model [12] in the work of Rinker. It is derived self-consistently in Perrot and Dharma-wardana's model.

To take into account the effect of non-Maxwellian electron distribution on inverse bremsstrahlung absorption, the Langdon correction on opacity [13] has been included by modifying the electron-ion collision frequency. For femtosecond-laser heating, this effect is less important since absorption occurs mainly at critical and supercritical densities where the collision frequency is comparable to the laser frequency.

For the hydrodynamic calculation, the quotidian equation of state (QEOS) of More *et al.* [14] is used. This model is based on a free energy conservation which combines a Thomas-Fermi description for the free electron energy with a Cowan model for the ion free energy. Near solid density, the Barnes correction is applied to yield zero total pressure and the experimentally observed bulk modulus. Nonlinear classical heat conduction is used in the fluid equation description. To ensure self-consistency, the thermal conductivity is derived from the same model as the electrical conductivity. Although a harmonic-mean flux limiter model [15] has been incorporated in our calculations, nonlocal flow is not important because of the extremely high plasma collision frequen-

1063-651X/95/51(6)/5208(4)/$06.00 51 R5208

cies at solid density. Even for 100-fs pulses and irradiances of 10^{15} W/cm^2, the effect of nonlocal heat flow is not evident for a flux limiter as low as 0.03.

For plasma produced by femtosecond lasers, the electron temperature may be much higher than the ion temperature. In the absence of theoretical or experimental data on the equation of state and transport coefficients of nonequilibrium dense plasmas, we have used only an equilibrium description. However, we will limit our discussion to 500-fs laser pulses at irradiances up to 10^{15} W/cm^2. Previous calculations of the self-reflectivity of the laser pump pulse in a similar regime have yielded reasonable agreement with observations [3].

For the irradiance of interest here, high-intensity effects such as profile modification by ponderomotive force [16], parametric instabilities and hot electron generation [17], and spatial dispersion and wave breaking [18] can be ignored. The maximum plasma temperature at the highest irradiance considered here is about 100 eV. Even if the plasma radiates as a blackbody, the power density of the frequency-integrated emission is about 1% of that of the laser radiation. The effect of radiation transport would therefore be minimal.

To illustrate the dominant mechanisms affecting the heat front at various times, Fig. 1 shows snapshots of the temperature profiles for a 400-nm, 500-fs (full width at half maximum) Gaussian laser pulse incident normally on an aluminum slab at an irradiance of 10^{15} W/cm^2. The wavelength of 400 nm corresponds to the second harmonic of the more popular Ti-sapphire lasers. The pulse length of 500 fs is chosen to allow the possibility of time-resolved diagnostics using a 100-fs probe pulse. The electrical and thermal conductivity model of Lee and More is used in our calculation. Time zero corresponds to the peak of the laser pulse. The heat fronts can be categorized into three temporal regimes with different characteristic features. On the rising edge of the laser pulse between −700 and −300 fs [Fig. 1(a)], heating becomes increasingly stronger but the temperature profiles retain similar spatial gradients. Near the peak of the laser pulse [Fig. 1(b)] steepening of the heat front can be seen. This is followed by a cooling phase on the falling edge of the laser pulse while the plasma on the front side of the target expands into the vacuum [Fig. 1(c)].

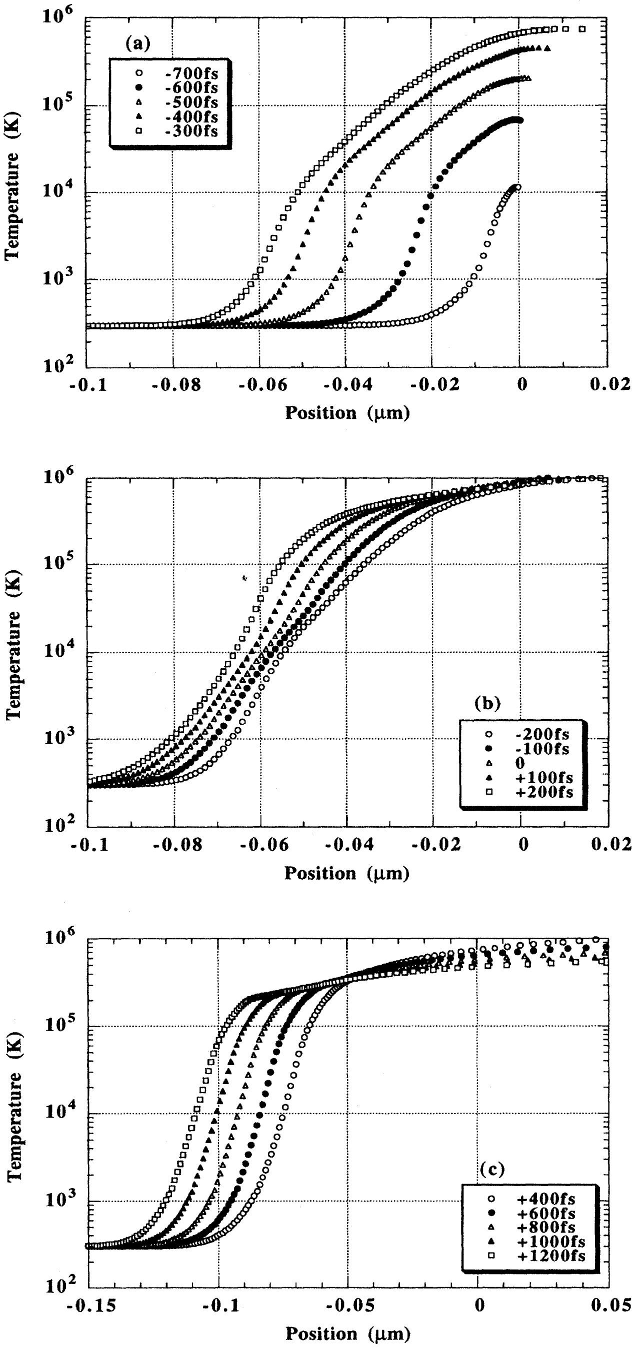

FIG. 1. Snapshots of temperature profiles at different times. The initial front surface of the target is at position zero. Laser is incident from the right.

On the rising edge of the laser pulse, the correlation between heat front and absorption of laser radiation as an evanescent wave can be seen from Figs. 1(a) and 2. For example, one may compare the snapshots at −300 fs. Within a depth of 100 Å from the target surface, the plasma temperature drops to about 5×10^5 K while laser absorption shows a rapid but nonexponential decrease. This can be traced to the temperature dependence of electrical conductivity (Fig. 3) and the nonlinear coupling between conductivity and heating. For the region between 100 and 400 Å, the plasma temperature varies between 5×10^5 and 4×10^4 K. The corresponding absorption profile shows a constant exponential gradient since the electrical conductivity remains approximately constant. As the plasma temperature drops to 10^3 K at 600 Å, the rapid and nonexponential decrease in laser absorption again reflects the temperature dependence of electrical conductivity. Below 10^3 K, the constant electrical conductivity assumed in the model yields another constant exponential decrease in the laser absorption profile. Accordingly, temporal variations in the heat front are the results of local heating by an evanescent wave whose intensity is increasing with time. This leads to an apparent propagation of the heat front.

In Fig. 2, we have also plotted the laser deposition profiles for times between −200 and 0 fs. These appear to be receding towards the target front surface. This indicates that the deposition process starts to decouple from the heat front as

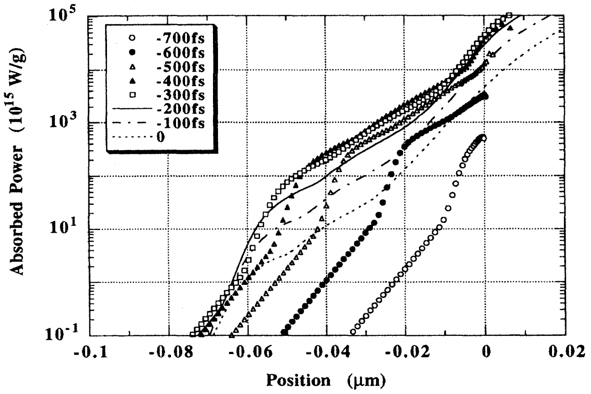

FIG. 2. Snapshots of laser deposition profiles.

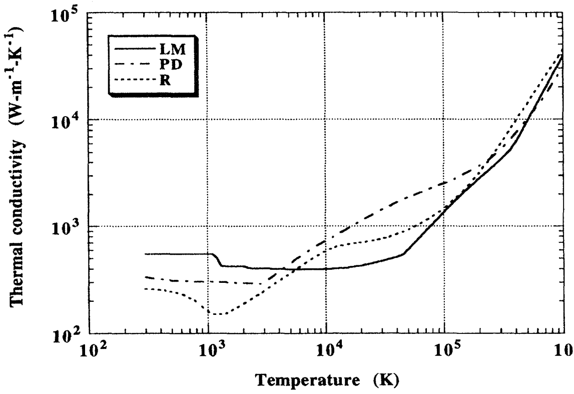

FIG. 4. Thermal conductivity as a function of temperature for aluminum at solid density. The data for Perrot and Dharma-wardana's model are obtained using the Wiedemann-Franz law.

absorption by the expanding plasma in the vacuum becomes dominant. At the same time, the temperature of the target front surface reaches a maximum [Fig. 1(b)] which enhances thermal conduction into the solid. The nonlinear thermal conductivity above 10^4 K (Fig. 4) leads to steepening of the heat fronts as displayed by the temperature profiles in Fig. 1(b). On the other hand, hydrodynamic effects also become noticeable. A compressional wave begins to form behind the heat front as shown in Fig. 5. At later times, the compressional wave coalesces with the heat front [Fig. 1(c)], giving rise to a shock wave. However, since the energy deposition process has already ceased, this shock wave will decay as it propagates into the solid.

Other calculations have been made for pulse lengths ranging from 100 to 500 fs and irradiances from 10^{14} to 10^{15} W/cm^2. The results show a similar behavior of the heat front as in the case discussed above.

To provide a more direct comparison with experiments, Fig. 6 shows the instantaneous velocity of the 10^4 K heat front as a function of time for three different plasma transport models. This isotherm is chosen because, in most materials, sufficient ionization will occur at this temperature to yield a critical density plasma for optical frequencies. Moreover, for the example presented here, this isotherm provides the clearest illustration of the dominant mechanisms governing the dynamics of the heat front. This latter aspect is of particular importance in the design and interpretation of experiments.

The first prominent feature of the velocity history is a broad peak between -700 and -300 fs. As discussed above, the change in temperature gradients during this period results from local heating by a laser field which is increasing in time. The apparent propagation of the heat front is dictated by the penetration of the laser field in the dense plasma, which is in turn dictated by the plasma electrical conductivity. For a broad range of temperatures between $\sim 10^4$ and 10^5 K, Lee and More's model yields the lowest conductivity values (Fig. 3). This lead to the least screening of the laser field and hence the highest apparent propagation velocity of the heat front. On the other hand, Rinker's model gives the highest conductivity values and thus the lowest propagation velocity.

At the end of this broad velocity peak, the laser deposition process begins to decouple from the heat front. This, together with the significant temperature rise on the target front surface, renders electron thermal conduction the dominant mechanism. The heat front is now driven by nonlinear ther-

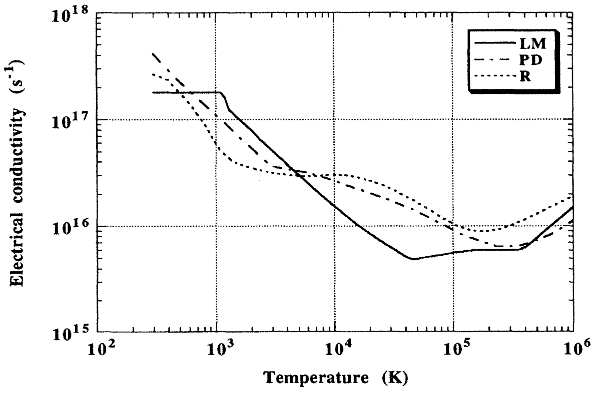

FIG. 3. Electrical conductivity as a function of temperature for aluminum at solid density. Only Rinker's model provides values down to room temperature. The electrical conductivity is assumed to be constant below 10^3 K in Lee and More's model. A simple linear extrapolation is used in Perrot and Dharma-wardana's model for temperatures below 2×10^3 K.

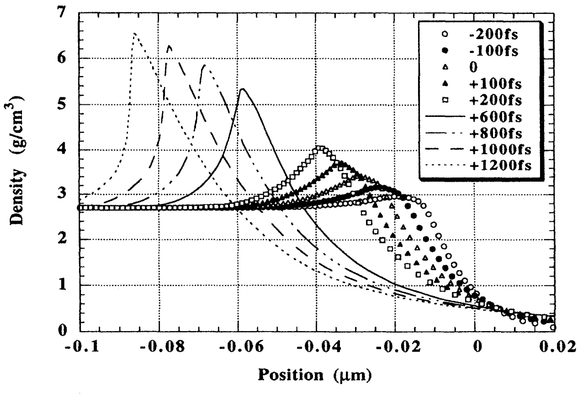

FIG. 5. Snapshots of density profiles in aluminum.

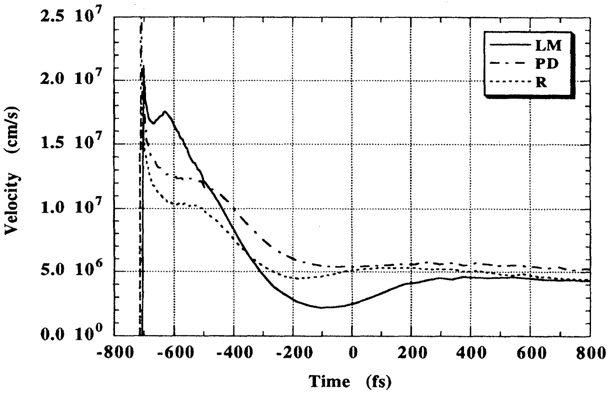

FIG. 6. Propagation speed of the 10^4 K isotherm as a function of time in aluminum for the models of Lee and More (LM) Perrot and Dharma-wardana (PD) and Rinker (R).

mal diffusion with increasing steepening of the thermal gradient. This accounts for the increase in velocity between -200 and $+200$ fs (Fig. 6). For temperatures of $\sim 10^4$–10^5 K, Lee and More's model yields the lowest thermal conductivity values, causing the heat front velocity to increase at the slowest rate. On the other hand, Perrot and Dharma-wardana's model gives the highest conductivity values, producing the strongest competing effect over the laser deposition process. At later times, the compressional wave induced by plasma expansion coalesces with the heat wave. The propagation is then dominated by hydrodynamic effects and becomes insensitive to plasma conductivities.

Also evident in Fig. 6 is the velocity spike at the very beginning in the formation of the heat front. This results from the combined effect of laser deposition and thermal conduction. However, such a short-lived transient is beyond the temporal resolution limit of current diagnostics.

In conclusion, results of our calculations have illustrated the important interplay between laser absorption, electron thermal transport, and hydrodynamics in the heating of a solid by intense femtosecond lasers. They have also clarified the mechanisms responsible for driving the heat front at various stages of its development. The latter finding leads to a more complete test of plasma transport theory. The velocity of a heat front can be obtained from Doppler shift measurements with 10-fs resolution [4]. If the sensitivity of the diagnostics can be extended to probe velocities of 10^6 cm/s, observations can be made to benchmark both electrical and thermal conductivity models as suggested by Fig. 6. Since an optical laser will not be able to probe a heat front inside a metal, a viable alternative it to generate the heat wave in silicon. With an energy band gap of 1.2 eV, silicon will exhibit a metallic behavior at the heat front at 10^4 K. On the other hand, the absorption constant of cold silicon is sufficiently low to allow an optical pulse to probe the heat front through the target rear surface (the $1/e$ absorption length at 800 nm is about 10 μm [19]). To avoid transmission of the intense femtosecond-laser pulse into the target before a plasma is formed, the target front surface can be coated with a 100-Å aluminum layer.

We wish to thank Y. T. Lee, R. M. More, F. Perrot, M. W. C. Dharma-wardana, and the Sesame Data Library for the conductivity modes. Many useful discussions with B. T. Vu, Y. T. Lee, R. M. More, F. Perrot, and M. W. C. Dharma-wardana are also acknowledged.

[1] H. M. Milchberg, R. R. Freeman, S. C. Davey, and R. M. More, Phys. Rev. Lett. **61**, 2364 (1988).

[2] R. Fedosejevs, R. Ottmann, R. Sigel, G. Kuhnle, S. Szatmari, and F. P Schäfer, Phys. Rev. Lett. **64**, 1250 (1990).

[3] A. Ng, P. Celliers, A. Forsman, R. M. More, Y. T. Lee, F. Perrot, M. W. C. Dharma-wardana, and G. A. Rinker, Phys. Rev. Lett. **72**, 3351 (1994).

[4] B. T. Vu, A. Szoke, and O. L. Landen, Phys. Rev. Lett. **72**, 3823 (1994).

[5] L. Spitzer, *Physics of Fully Ionized Gases* (Interscience, New York, 1962).

[6] M. Born and E. Wolf, *Principles of Optics* (Pergamon, Oxford, 1980), p. 51.

[7] P. Celliers, Ph.D. thesis, University of British Columbia, 1988 (unpublished).

[8] Y. T. Lee and R. M. More, Phys. Fluids **27**, 1273 (1984).

[9] Sesame Data Table material no. 23713 [G. A. Rinker, Phys. Rev. B **31**, 4207 (1985); **31**, 4220 (1985)].

[10] F. Perrot and M. W. C. Dharma-wardana, Phys. Rev. A **36**, 238 (1987).

[11] W. A. Lokke and W. H. Grasberger, Lawrence Livermore National Laboratory Report No. UCRl-52276, 1977 (unpublished).

[12] D. A. Liberman, Phys. Rev. B **20**, 4981 (1979); J. Quant. Spectrosc. Radiat. Transfer **27**, 335 (1982).

[13] A. B. Langdon, Phys. Rev. Lett. **44**, 575 (1980).

[14] R. M. More, K. H. Warren, D. A. Young, and B. G. Zimmerman, Phys. Fluids **31**, 3059 (1988).

[15] R. C. Malone, R. L. McCrory, and R. L. More, Phys. Rev. Lett. **34**, 721 (1975).

[16] D. W. Forslund, J. M. Kindel, K. Lee, and E. L. Lindman, Phys. Rev. Lett. **36**, 35 (1976).

[17] P. K. Kaw, W. L. Kruer, C. S. Liu, and K. Nishikawa, *Advances in Plasma Physics* (Wiley, New York, 1976), Vol. 16.

[18] S. C. Rae and K. Burnett, Phys. Rev. A **44**, 3853 (1991).

[19] W. C. Dash and R. Newman, Phys. Rev. **99**, 1151 (1955).